Provided for non-commercial research and education use.
Not for reproduction, distribution or commercial use.

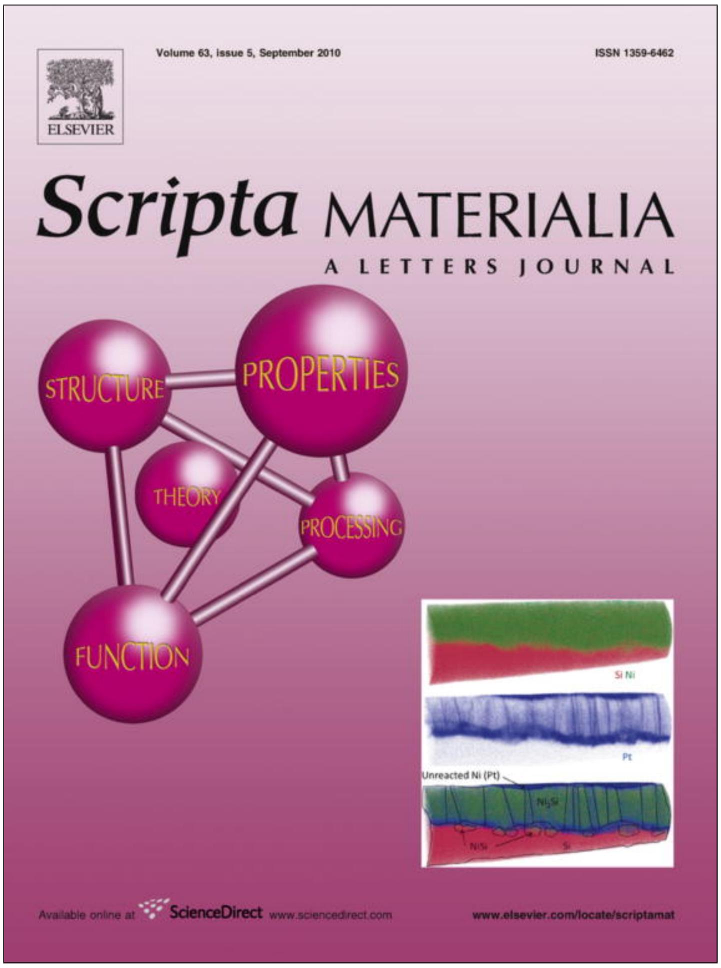
Volume 63, issue 5, September 2010
ISSN 1359-6462
ELSEVIER
Scripta MATERIALIA
A LETTERS JOURNAL
STRUCTURE
PROPERTIES
THEORY
PROCESSING
FUNCTION
Si Ni
Pt
Unreacted Ni (Pt)
Ni2Si
NiSi
Si
Available online at ScienceDirect www.sciencedirect.com
www.elsevier.com/locate/scriptamat

This article appeared in a journal published by Elsevier. The attached copy is furnished to the author for internal non-commercial research and education use, including for instruction at the authors institution and sharing with colleagues.

Other uses, including reproduction and distribution, or selling or licensing copies, or posting to personal, institutional or third party websites are prohibited.

In most cases authors are permitted to post their version of the article (e.g. in Word or Tex form) to their personal website or institutional repository. Authors requiring further information regarding Elsevier's archiving and manuscript policies are encouraged to visit:

http://www.elsevier.com/copyright

Available online at www.sciencedirect.com

ScienceDirect

Scripta Materialia 63 (2010) 512–515

Scripta MATERIALIA

www.elsevier.com/locate/scriptamat

# Measurement of residual stress field anisotropy at indentations in silicon

Yvonne B. Gerbig,[a,*] Stephan J. Stranick[b] and Robert F. Cook[a]

[a]*Ceramics Division, National Institute of Standards and Technology, Gaithersburg, MD 20899, USA*
[b]*Surface and Microanalysis Science Division, National Institute of Standards and Technology, Gaithersburg, MD 20899, USA*

Received 21 April 2010; accepted 13 May 2010
Available online 16 May 2010

The residual stress field around spherical indentations on single-crystal silicon of different crystallographic orientations is mapped by Raman microscopy. All orientations exhibit an anisotropic stress pattern with an orientation specific symmetry that can be related to the number and type of the active $\{111\}\langle 110 \rangle$ slip systems. Residual compressive stress is concentrated in lobes oriented along the projection onto the indented plane of the activated slip plane normal and tensile stress regions are arranged alternating with the compressive stress lobes.
Published by Elsevier Ltd. on behalf of Acta Materialia Inc.

*Keywords:* Nanoindentation; Raman spectroscopy; Silicon; Residual stresses

Residual stress states arising from constrained localized deformation are critical in determining the manufacturing yield and operational performance of many advanced silicon (Si)-based devices [1,2]. Deposition strains and thermal expansion mismatch effects arising from disparate materials in close proximity can generate purely elastic residual stresses that alter the Si electronic band structure [3,4]. In solid-state electronics, infrared optical and photovoltaic devices this effect can compromise device functionality by altering carrier mobility and optical absorption characteristics [5,6], although deliberate "stress engineering" can also be used to enhance or tune device performance [7,8]. If such stresses, intended or otherwise, become great enough they can initiate dislocations in the Si and subsequent plastic deformation, with usually degrading effects. Conversely, the localized plastic deformation zones produced at small-scale surface contacts generate residual stress states in the surrounding elastic matrix. In microelectromechanical systems (MEMS), particularly those with moving, contacting parts, this effect can compromise device reliability by leading to the initiation of cracks and component failure. Hence, in order to optimize the yield and performance of Si devices, measurements of residual stress states are critical [9].

In this work, residual stress fields around plastic indentations in Si single crystals of three crystallographic orientations are investigated. The indentations are direct models of the contact flaws that limit the reliability of MEMS components and are good test vehicles for assessing crystallographic effects in stress-engineered devices. The residual stress fields are mapped by confocal Raman microscopy (CRM), which has become a widely established technique for analyzing stress distributions at the nanoscale with suitable resolution, both spatially and in terms of stress [10–13]. The study extends that of a previous work [14] in mapping the residual stress field in much greater detail and with greater surface sensitivity.

Instrumented indentation is a widely used technique to study the mechanical behavior of diamond cubic Si at small scales and thus has been exploited in particular as a model for processes such as deformation and fracture occurring in micromachining [15–19]. Plastic deformation of Si single crystals in indentation experiments is accomplished by dislocation activity and multiple-step transformations to various high-pressure phases [14,20,21]. Over the last few years, various contact models for Si indentation have been proposed to describe the average thickness and approximate shape of the transformed zone [22,23] and even the distribution of specific high-pressure phases within this zone [16,24]. However, these models

---

[*] Corresponding author. Address: National Institute of Standards and Technology, Ceramics Division, 100 Bureau Drive, Gaithersburg, MD 20899, USA; e-mail: yvonne.gerbig@nist.gov

1359-6462/$ - see front matter Published by Elsevier Ltd. on behalf of Acta Materialia Inc.
doi:10.1016/j.scriptamat.2010.05.017

assume an isotropic deformation behavior and stress distribution for single-crystal Si. But is this assumption really applicable? Anisotropic arrangements of dislocation loops (dislocation rosettes) have been observed in previous indentation experiments on Si(111) and Si(100) samples [25–28]. As a consequence, anisotropy in deformation and residual stress seems likely. Plastically deformed regions of complex three-dimensional shape were found for indented Si(111) surfaces but a spherical stress field during indentation was considered [17]. This is contradicted by the CRM observations on Si(100), Si(110) and Si(111) [14], X-ray diffraction studies [29] and finite element method simulations [18], all of which provide evidence of an anisotropic stress distribution around indentations in Si.

The test samples in this study were 3 mm thick × 35 mm diameter, parallel sided, polished Si(001), Si(110) and Si(111) disks used previously [14]. The samples were indented with a conospherical diamond probe with a nominal radius of 5 μm at room temperature in a nitrogen-rich atmosphere (temperature: 21 ± 1 °C, relative humidity: 5 ± 1%). A conospherical probe was used so as to not introduce indentation symmetries that might conflict with those of the sample crystal structure. Furthermore, the risk of affecting the stress field around the indentation by crack initiation, as observed for indentations with pyramidal indenters [19,30,31], is reduced. The indenter was displaced perpendicular to the Si(001), Si(110) and Si(111) surfaces of the disks, resulted in loading along the Si[$00\bar{1}$],Si[$\bar{1}\bar{1}0$]and Si[$\bar{1}\bar{1}\bar{1}$] directions. During indentation the load was linearly increased with time to the maximum value of 80 mN, held for 5 s, and linearly decreased; the loading and unloading rates were 5 mN $s^{-1}$. This peak load deformed the material plastically (combined with phase transformation) at the indentation site without generating cracks, as previous tests have shown [14].

Hyperspectral CRM was used to map the phonon Raman scattering peak shift resulting from the mechanically induced strain adjacent to the plastic deformation impressions in the disks. The CRM instrument and mapping procedures were those used previously [14] with the following exceptions: an optically pumped semiconductor laser with a wavelength of 488 nm was used for excitation. The information depth for this wavelength is nominally 250 nm for Si, providing greater surface sensitivity than previously. The illumination power was set to 1 mW at the sample surface with the polarization axis aligned along the ⟨ 110 ⟩ direction for Si(001) and ⟨ 112 ⟩ direction for Si(111) and Si(110). As previously, a shift in the Raman peak of the longitudinal optical phonon from its zero stress value of approximately 520.5 $cm^{-1}$ to smaller frequencies is interpreted as a tensile strain or stress and to greater frequencies as a compressive strain or stress [10,13,32].

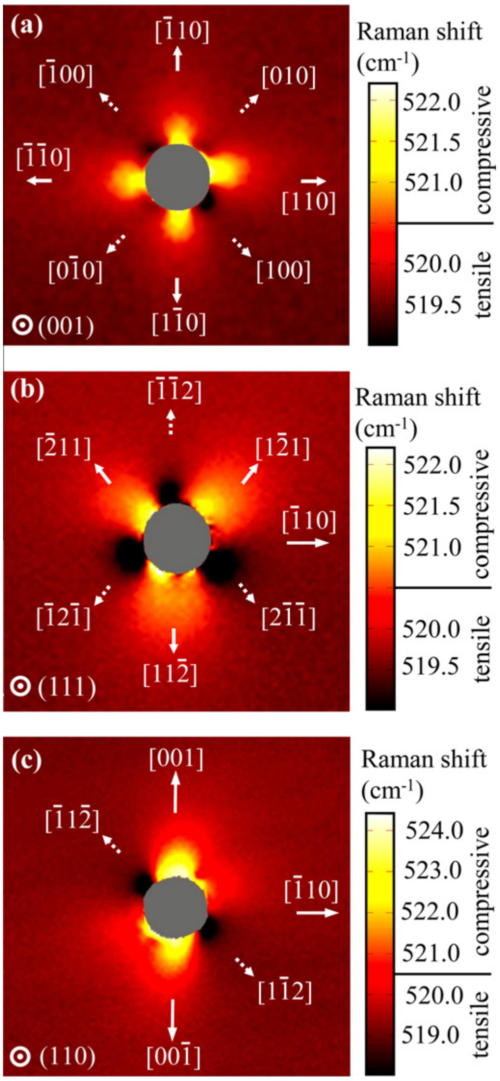

**Figure 1.** Residual stress field mapped by CRM of single-crystal Si indented perpendicular to (a) Si(001), (b) Si(111) and (c) Si(110) surface plane. Scan sizes: 12.5 μm × 12.5 μm.

Figure 1 shows the residual stress maps obtained from the CRM data, revealing symmetric, anisotropic patterns of alternating compressive and tensile stress lobes adjacent to the contact impression for all three tested orientations. The impressions are indicated by grayed-out disks from which data were excluded; the presence of multiple Si phases in the impressions hinders straightforward data collection and analysis. The residual stress fields decreased significantly in intensity with increasing distance from the impressions. The symmetry of the stress field is specific to the crystallographic orientation and direction of mechanical loading of the indented Si single crystal. For the (001) surface, a fourfold stress pattern is observed (Fig. 1a). The compressive stress lobes are located along the ±[110] and ±[$\bar{1}10$] directions, whereas tensile strain is detected between the regions of compressive stress along the ±[100] and ±[010] directions. For the (111) surface, a threefold pattern is observed (Fig. 1b) with the compressive stress lobes extending in the [$\bar{2}11$],[$1\bar{2}1$], and [$11\bar{2}$] directions and tensile lobes extending in the reverse directions. This observation is in good agreement with stress maps reported for this orientation in previous works with pyramidal indenters [29,32]. For the Si(110) surface, a near twofold symmetry pattern is observed (Fig. 1c), with compressive stress lobes extending predominantly in the ±[001] directions and tensile lobes appearing in the near ±[$1\bar{1}2$] directions. Not shown here, for a given orientation the symmetry of the residual stress field did not change significantly with increasing indentation load, as long as cracking did not occur, whereas the local stress value did change and the stress field extended farther from the impression.

The irreversible indentation deformation of Si single crystals occurs by simultaneous dislocation activity and phase transformation [23], with the phase transformation becoming the dominant component with increasing indentation load [33,34]. During indentation loading, diamond cubic Si (Si-I) transforms to the $\beta$-tin phase (Si-II) [35], which undergoes further transformations to other high-pressure phases (Si-III, Si-XII), an amorphous phase or a mixture thereof during unloading [35,36]. If the shear stress induced by the indenter exceeds the critical threshold for slip in Si, crystallographic translation of material is initiated parallel to activated slip planes causing a distortion of the crystal structure along the slip directions and, at greater indentation loads, additional dislocations [33,37]. As the contact and loading conditions are similar to studies in which slip bands and dislocations have been observed [33,37], such defects are most likely to be present in the samples tested here.

Dislocations and slip are bound to the slip systems dictated by the crystal structure. For the Si-I structure, the slip systems are similar to those of face centered cubic crystal systems, $\{111\}$ slip planes and $\langle 110 \rangle$ slip directions [38]. Perfect dislocations in this system have Burgers vector, $\boldsymbol{b} = (a/2)\langle 110 \rangle$, where $a$ is the Si-I lattice constant, with common dislocation line directions of $\langle 110 \rangle$ at 60° to the Burgers vector. Such 60° dislocations can separate into 30 and 90° partial dislocations with $\boldsymbol{b} = (a/6)\langle 112 \rangle$. Three modes of dislocation motion are identified at indentations in Si-I structures: Dislocations with $\boldsymbol{b}$ inclined to the indented surface that move into the crystal on $\{111\}$ planes (i) converging or (ii) diverging beneath the indenter, and (iii) dislocations with $\boldsymbol{b}$ parallel to the indented surface that spread primarily parallel to the surface outward from the indenter [39]. Dislocations in (i) entangle on the intersecting slip planes and, if split into partials, the leading 30° partials can combine to form Lomer–Cottrell locks; such a system work hardens rapidly and thus does not contribute much to the indentation deformation, although could be crucial in initiating phase transformations to accommodate the deformation. Molecular dynamics simulations indicate that the high-pressure phases are located along $\langle 110 \rangle$ directions as the phase transformation is initiated by an inhomogeneous distortion of tetrahedral bonding in the slip direction [40]. The crystallographic structures of the Si-I phase and the transformed phases differ significantly leading to a severely distorted interface along the $\{111\}$ planes [41]. Dislocations in (iii) are responsible for extended rosette patterns and are largely suppressed at room temperature. Hence, most of the indentation deformation occurs through the action of slip system (ii). The residual stress field external to the contact impression thus arises in reaction to the strain generated by phase transformation events directly beneath the contact impression [33,37] and, predominantly, dislocation motion on divergent slip planes exterior to the transformation zone. The symmetry of the residual stress field will reflect the symmetry of the slip processes.

The active slip systems among the 12 possible were identified by calculating the Schmid factor (Table 1) for each system, where the Schmid factor is $\cos\varphi \times \cos\lambda$, $\varphi$ is the angle between the loading direction and normal to the slip plane, and $\lambda$ is the angle between the loading direction and the slip direction, here taken as $\boldsymbol{b}$. The greater the absolute value of the Schmid factor the greater is the resolved shear stress and the probability of slip. Table 1 shows that only two of three possible slip systems were active on each of the unique slip planes and that four planes were active for the (001) orientation, three for (111) and two for (110). The active slip systems are indicated in Figure 2: the coordinate system indicates the crystallographic orientation (corresponding to Figure 1) and the schematic diagram represents the projection of the slip plane and active Burgers vectors onto the indentation plane. For example, $(\bar{1}\bar{1}1)$ is common to all three orientations as an active slip system with two active (perfect) Burgers vectors of $\boldsymbol{b} = [\bar{1}0\bar{1}]$ and $[0\bar{1}\bar{1}]$ and a dislocation line direction of $[\bar{1}10]$.

**Table 1.** Schmid factor for various loading directions of diamond cubic Si.

| Slip plane | Burgers vector direction | Schmid factor magnitude forloading direction: | | |
|---|---|---|---|---|
| | | $[00\bar{1}]$ | $[\bar{1}\bar{1}\bar{1}]$ | $[\bar{1}\bar{1}0]$ |
| $(\bar{1}\bar{1}1)$ | $[\bar{1}0\bar{1}]$ | 0.408 | 0.272 | 0.408 |
| | $[0\bar{1}\bar{1}]$ | 0.408 | 0.272 | 0.408 |
| | $[\bar{1}10]$ | 0 | 0 | 0 |
| $(1\bar{1}1)$ | $[0\bar{1}\bar{1}]$ | 0.408 | 0.272 | 0 |
| | $[10\bar{1}]$ | 0.408 | 0 | 0 |
| | $[110]$ | 0 | 0.272 | 0 |
| $(\bar{1}11)$ | $[\bar{1}0\bar{1}]$ | 0.408 | 0.272 | 0 |
| | $[01\bar{1}]$ | 0.408 | 0 | 0 |
| | $[110]$ | 0 | 0.272 | 0 |
| $(111)$ | $[01\bar{1}]$ | 0.408 | 0 | 0.408 |
| | $[10\bar{1}]$ | 0.408 | 0 | 0.408 |
| | $[\bar{1}10]$ | 0 | 0 | 0 |

The physical picture that emerges is that indentation deformation is accommodated by the motion of material by dislocation slip away from the indentation in directions perpendicular to the moving dislocation lines. When projected onto the indentation plane on which measurements were performed for the example given, this is the $[\bar{1}\bar{1}0]$ direction for the (001) indentation plane, the $[11\bar{2}]$ direction for (111) and the $[00\bar{1}]$ direction for (110). This motion of material leads to compression in these directions and the symmetric equivalents, in agreement with the observations of Figure 1: $\pm[110]$ and $\pm[\bar{1}10]$ for (001); $[\bar{2}11]$,$[1\bar{2}1]$ and $[11\bar{2}]$ for (111); and $\pm[001]$ for (110). Lobes of tensile stress are then simply generated between the compressive lobes in reaction to this motion of material. In this view, in which the physical process is one of indentation accommodation by slip on selected planes in selected directions, it would be expected that the compressive stress field would best reflect the symmetry of the predominant slip system. It would also be expected that decreasing the symmetry of the predominant slip system would lead to decreased constraint on other secondary systems and a breakdown of the symmetry of the overall residual field. Figure 1 is consistent with such a view: the compressive lobes are the best defined feature of the residual field and the (110) orientation in particular has clear indications of deviations from twofold mirror symmetry.

In summary, crystallographic orientation significantly influences the distribution of in-plane residual stress adja-

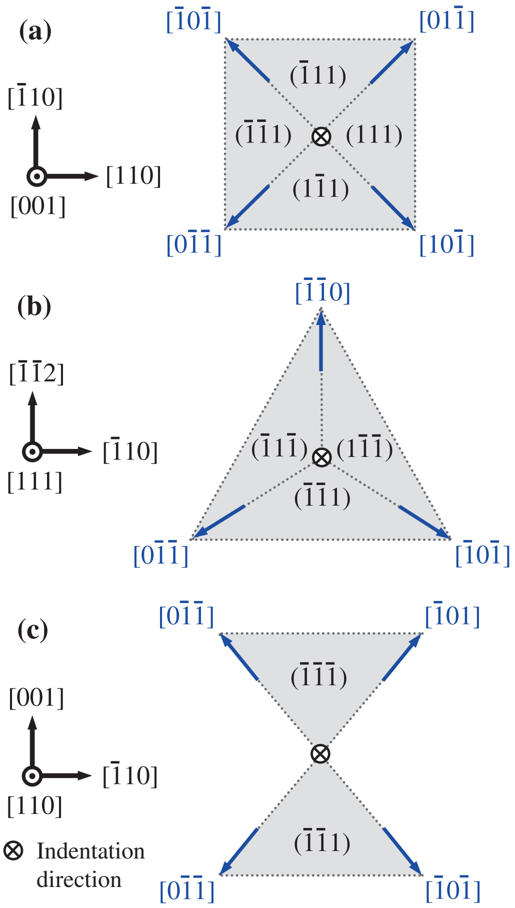

**Figure 2.** Active slip planes projected onto indented surface planes (a) Si(001), (b) Si(111) and (c) Si(110). The slip planes are highlighted in grey. The active Burgers vectors are indicated by blue arrows. The coordinate systems indicated are those used in. (For interpretation of the references to colour in this figure legend, the reader is referred to the web version of this article.)

cent to spherical indentations in Si single crystals. All three orientations measured exhibited a specific, symmetrical stress signature related to the orientation and number of activated $\{111\}\langle 110 \rangle$ slip systems of the Si-I structure in accordance with the Schmid rule. Compressive stress was concentrated in lobes in directions of the projection of the slip plane normal, and direction of dislocation line motion, onto the indented plane. Tensile stress regions were arranged alternating with the compressive stress lobes. As tensile stresses are responsible for crack initiation and propagation, the anisotropic distributions of tensile stress are of particular importance and suggest strong crystallographic effects in the driving force for fracture at contacts. Such driving forces are superposed on strong crystallographic effects in the fracture resistance of Si [19], suggesting that contact-induced crack initiation and propagation in MEMS components, and thus the reliability of MEMS devices, will have complex crystallographic dependencies. Similar crystallographic complexities will also exist in stress-engineered structures. Finally, it is obvious that the in-plane stress field around and, one can conclude, also within the impression is an anisotropic one, and needs to be considered as such in future approaches of fundamental modeling of the contact mechanics of Si single crystal surfaces.

[1] R.H. Krondorfer, Y.K. Kim, IEEE Trans. Compon. Packag. Technol. 30 (2007) 285.
[2] D.F. Bahr, B.T. Crazier, C.D. Richards, R.F. Richards, ASTM Spec. Tech. Publ. 1413 (2001) 28.
[3] S. Miyazaki, M. Narasaki, A. Suyama, M. Yamaoka, H. Murakami, Appl. Surf. Sci. 216 (2003) 252.
[4] S. Park, Y. Ishikawa, K. Wada, Y. Tsusaka, J. Matsui, Jpn. J. Appl. Phys. 48 (2009) 064501.
[5] M.V. Fischetti, S.E. Laux, J. Appl. Phys. 80 (1996) 2234.
[6] Z.T. Kuznicki, M. Ley, Appl. Phys. Lett. 82 (2003) 4241.
[7] B. Ghyselen, Mater. Sci. Eng. B. 16 (2005) 124.
[8] M. Chu, Y. Sun, U. Aghoram, S.E. Thompson, Annu. Rev. Mater. Res. 39 (2009) 203.
[9] V.T. Srikar, S.M. Spearing, Exp. Mech. 43 (2003) 238.
[10] I. De Wolf, Semicond. Sci. Technol. 11 (1996) 139.
[11] U. Schmidt, W. Ibach, J. Müller, K. Weishaupt, O. Hollricher, Vib. Spectrosc. 42 (2006) 93.
[12] J.W. Pomeroy, Gkotsis, M. Zhu, G. Leighton, Kirby, M. Kuball, J. Microelectromech. Syst. 17 (2008) 1310.
[13] M.D. Vaudin, Y.B. Gerbig, S.J. Stranick, R.F. Cook, Appl. Phys. Lett. 93 (2008) 193116.
[14] Y.B. Gerbig, S.J. Stranick, D.J. Morris, M.D. Vaudin, R.F. Cook, J. Mater. Res. 24 (2009) 1172.
[15] B.P. O'Connor, E.R. Marsh, J.A. Couey, Prec. Eng. 29 (2005) 124.
[16] T. Kiriyama, H. Harada, J. Yan, Semicond. Sci. Technol. 25 (2009) 025014.
[17] M. Yoshioka, K. Kawamura, J. Appl. Phys. 75 (1994) 2367.
[18] M. Yoshino, T. Aoki, N. Chandrasekaran, T. Shirakashi, R. Komanduri, Int. J. Mech. Sci. 43 (2001) 313.
[19] R.F. Cook, J. Mater. Sci. 41 (2006) 841.
[20] I.V. Gridneva, V. Yu, V. Milman, V.I. Trefilov, Phys. Status Solidi A 14 (1972) 177.
[21] A.P. Gerk, D. Tabor, Nature 271 (1978) 732.
[22] B.A. Galanov, V. Domnich, Y. Gogotsi, Exp. Mech. 43 (2003) 303.
[23] L.J. Vandeperre, F. Giuliani, S.J. Llloyd, W.J. Clegg, Acta Mater 55 (2007) 6307.
[24] T. Vodenitcharova, L.C. Zhang, Int. J. Solids Struct. 40 (2003) 2989.
[25] V.G. Eremenko, V.I. Nikitenko, Phys. stat. sol. (a) 14 (1972) 317.
[26] H. Harada, K. Sumino, J. Appl. Phys. 53 (1982) 4838.
[27] M.J. Hill, D.J. Rowcliffe, J. Mater. Sci. 9 (1974) 1569.
[28] S.M. Hu, J. Appl. Phys. 46 (1975) 1470.
[29] T. Iizuka, Y. Okada, Jpn. J. Appl. Phys. 33 (1994) 1435.
[30] M. Bowden, D.J. Gardiner, Appl. Spectrosc. 51 (1997) 1405.
[31] A.J. Huber, A. Ziegler, T. Köck, R. Hillenbrand, Nat. Nanotechnol. 4 (2008) 153.
[32] Puech, F. Demangeot, P.S. Pizani, V. Domnich, Y. Gogotsi, J. Phys. Condens. Matter. 16 (2004) S9.
[33] J.E. Bradby, J.S. Williams, J. Wong-Leung, M.V. Swain, Munroe, J. Mater. Res. 16 (2001) 1500.
[34] A.J. Haq, P.R. Munroe, J. Mater. Res. 24 (2009) 1967.
[35] V. Domnich, Y. Gogotsi, Rev. Adv. Mater. Sci. 3 (2002) 1.
[36] D. Ge, V. Domnich, Y. Gogotsi, J. Appl. Phys. 93 (2003) 2418.
[37] H. Saka, A. Shimatani, M. Suganuma, Suprijadi, Phil. Mag. A 82 (2002) 1971.
[38] N.S. Brar, W.R. Tyson, Scr. Metall. 6 (1972) 587.
[39] S.G. Roberts, P.D. Warren, P.B. Hirsch, J. Mater. Res. 1 (1986) 162.
[40] D.E. Kim, S.I. Oh, Nanotechnol 17 (2006) 2259.
[41] Y.Q. Wu, X.Y. Yang, Y.B. Xu, Acta Mater 47 (1999) 2431.